# nature materials

**Article** 

https://doi.org/10.1038/s41563-023-01644-8

# Large-scale optical characterization of solid-state quantum emitters

Received: 11 October 2022

Accepted: 18 July 2023

Published online: 21 August 2023



Madison Sutula <sup>1</sup> □, Ian Christen¹, Eric Bersin <sup>1</sup>², Michael P. Walsh¹, Kevin C. Chen ¹, Justin Mallek², Alexander Melville², Michael Titze ³, Edward S. Bielejec³, Scott Hamilton², Danielle Braje ², P. Benjamin Dixon ² & Dirk R. Englund ¹

Solid-state quantum emitters have emerged as a leading quantum memory for quantum networking applications. However, standard optical characterization techniques are neither efficient nor repeatable at scale. Here we introduce and demonstrate spectroscopic techniques that enable large-scale, automated characterization of colour centres. We first demonstrate the ability to track colour centres by registering them to a fabricated machine-readable global coordinate system, enabling a systematic comparison of the same colour centre sites over many experiments. We then implement resonant photoluminescence excitation in a widefield cryogenic microscope to parallelize resonant spectroscopy, achieving two orders of magnitude speed-up over confocal microscopy. Finally, we demonstrate automated chip-scale characterization of colour centres and devices at room temperature, imaging thousands of microscope fields of view. These tools will enable the accelerated identification of useful quantum emitters at chip scale, enabling advances in scaling up colour centre platforms for quantum information applications, materials science and device design and characterization.

Quantum emitters play a central role in quantum information science and technology  $^{1,2}$ . Colour centres in solids have emerged as a leading platform for quantum information processing, with applications in sensing, computation and communication. Their electron spin degree of freedom can store quantum states for milliseconds to seconds  $^{3,4}$ , and can be efficiently transduced into a flying qubit via a coherent spin–photon interface. These light–matter interactions can be engineered with cavity quantum electrodynamics  $^{5,6}$ , accessible through nanofabrication  $^{7-12}$  and heterogeneous integration techniques  $^{13-17}$ . Nuclear spin ancilla qubits provide additional degrees of freedom  $^{18}$ , enabling longer storage times  $^{19}$ , local multiqubit logic protocols such as error detection and correction  $^{20,21}$  and potential for more robust computation such as brokered entanglement  $^{22}$  or cluster-state generation  $^{23}$ .

In spite of these promising properties and early demonstrations, most approaches rely on the integration and control of a single colour

centre at each node <sup>24–26</sup>. However, quantum information processing nodes will require many individually addressable quantum emitters, each with long-lived spin states and a high-quality photonic interface <sup>27</sup>. A critical challenge faced by colour centre qubits, especially compared with neutral-atom and trapped-ion qubit architectures, is spectral inhomogeneity <sup>28</sup>. Although a number of techniques have been demonstrated to practically or theoretically overcome this inhomogeneity, including retuning emitter transitions via Stark <sup>29</sup> or strain tuning <sup>30</sup>, compensating for differential phase accumulation <sup>31</sup>, and shifting the emitted photons by optical frequency conversion <sup>22</sup> or frequency modulation <sup>33</sup>, each of these solutions relies on the precharacterization of the optical transitions involved. Additionally, up to now, approaches to understand the range of colour centre performance and uniformity have been limited to ensemble-level statistics, obscuring the individual colour centre properties. Scaling up the number of solid-state quantum

<sup>1</sup>Research Laboratory of Electronics, Massachusetts Institute of Technology, Cambridge, MA, USA. <sup>2</sup>Lincoln Laboratory, Massachusetts Institute of Technology, Lexington, MA, USA. <sup>3</sup>Sandia National Laboratories, Albuquerque, NM, USA. —e-mail: mmsutula@mit.edu

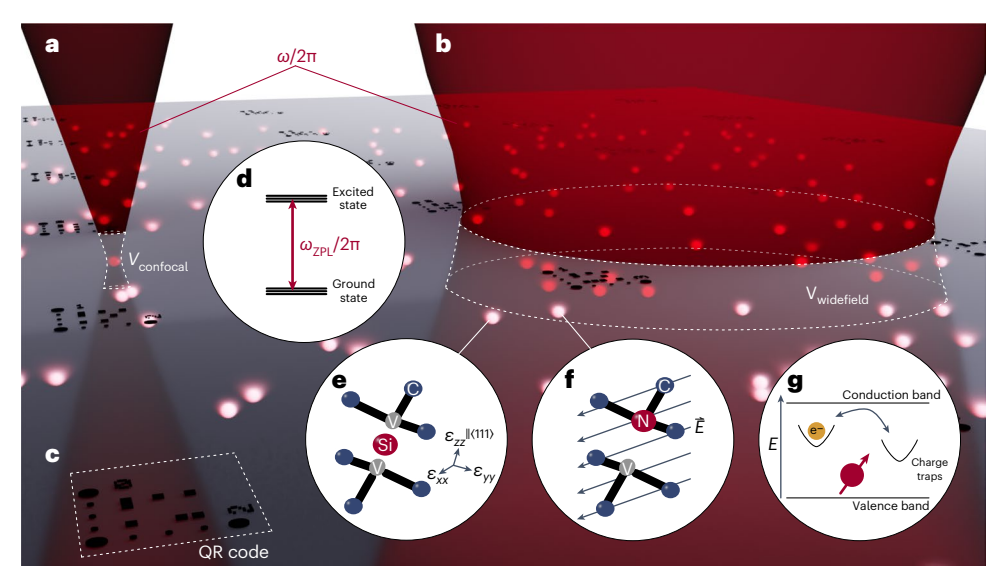


**Fig. 1**| **Techniques for chip-scale characterization. a**, Standard confocal microscopy enables spectroscopy on a diffraction-limited volume  $V_{\rm confocal}$ , **b**, Our widefield microscopy technique (Supplementary Section 2) allows for simultaneous parallelized spectroscopic measurements over many colour centres in a larger sample volume  $V_{\rm widefield}$ , **c**, We fabricate QR-style codes onto the surface of our samples as a spatial reference frame, which we convolutionally decode in real time, enabling us to track and revisit the colour centres.

d-g, Together, these techniques allow us to probe the optical transitions of colour centres  $(\boldsymbol{d})$ , including perturbations such as local strain environment  $(\boldsymbol{e})$ , which the SiV (pictured) is particularly sensitive to; electric fields  $(\boldsymbol{f})$ , which the NV (pictured) is particularly sensitive to; and the time-varying occupancy of charge traps in the crystal host  $(\boldsymbol{g})$ , which is thought to cause inhomogeneous line broadening.

memories accessible in quantum information processing systems requires large-scale characterization techniques to identify the most viable qubits for practical use.

Here we report on a high-throughput approach for the spectroscopy and synthesis of quantum emitters, while retaining single-emitter resolution, on diamond colour centres (Fig. 1). We track colour centres by registering them to a fabricated, machine-readable global coordinate system, enabling the systematic comparison of individual colour centre sites over many experiments, which is critical for understanding the role of materials processing<sup>34</sup>. We then implement resonant photoluminescence excitation (PLE) in a widefield cryogenic microscope to realize two orders of magnitude speed-up over confocal microscopy. Finally, we demonstrate the automated chip-scale characterization of colour centres and devices at room temperature, imaging thousands of microscope fields of view (Supplementary Videos 1–5).

With the large datasets accessible through widefield PLE, we identify a sample with an exceptionally narrow inhomogeneous distribution of silicon-vacancy centres in diamond (SiVs), and we verify in a sample implanted via focused ion beam (FIB) that the optical properties of highly strained SiVs do not degrade. These techniques provide a paradigm in which the optical properties of individual colour centres can be identified, tracked and categorized. We anticipate that the reported high-throughput tools will close the loop between materials processing and spectroscopy, enabling the development of scalable quantum information processors.

#### Results

### Registering colour centres to fabricated markers

Scanning confocal microscopy is a standard technique used to identify colour centres, revealing bright spots located relative to the coordinates set by the scanning axes of the microscope. However, returning to a previously characterized set of emitters on a chip can be challenging due to the vast difference between the  $\mathcal{O}(100~\mu m \times 100~\mu m)$  size of the field of view and the  $\mathcal{O}(5~mm \times 5~mm)$  size of the chip, especially after the frame of reference is lost due to sample removal. Previous work has used bright 'lodestar' emitters or image-stitching techniques

to return to a given set of emitters<sup>35</sup>, although these techniques are not general, as all the samples do not possess sufficiently unique features for each field of view of interest.

We demonstrate the ability to register emitters to a global coordinate system using a standard home-built cryogenic confocal microscope setup. This technique enables us to revisit the same set of nitrogen-vacancy centres in diamond (NVs) over the course of multiple cooling cycles and therefore to track the emitter properties over time. We first fabricate quick response (QR)-style codes on the surface of the diamond chip (see the 'Diamond fabrication' section). We choose to use QR codes over other options such as numerics or lettering for their ability to be quickly deconvolved and decoded, as well as their compatibility with checksum-type error correction, which improves robustness against decoding errors caused by fabrication errors, damage or physical debris. These are decoded in real time with custom image processing tools by establishing a coordinate transform between the global sample coordinates and the local microscope coordinates using the region of sample space in view of the scanning confocal microscope (Fig. 2a).

We use off-resonant scanning fluorescence microscopy under 515 nm excitation to image a low density of NV centres on the surface of the chip. To create these fluorescent centres, the chip was implanted with  $1 \times 10^9$  cm<sup>-2</sup> of <sup>15</sup>N ions at 185 keV, and subsequently annealed at 1,200 °C in an ultrahigh vacuum, tri-acid cleaned in a 1:1:1 mixture of nitric, perchloric and sulfuric acids by boiling for 1 h (ref. 36) and finally cleaned in a 3:1 sulfuric acid:hydrogen peroxide piranha solution. We classify bright, diffraction-limited spots as candidate emitter sites (Fig. 2a, inset). We then determine the spectral positions and linewidths of the zero-phonon line (ZPL) optical transitions at each candidate site with PLE spectroscopy. To do this, we measure the fluorescence response of each emitter by scanning a resonant laser over the ZPL transitions and collecting light emitted into the phonon sideband on an avalanche photodiode. We label the spin-conserving transitions associated with  $m_s = 0$  by mean ZPL frequency  $\bar{\omega} = 1/2(E_x + E_y)$  and splitting  $\delta = |E_v - E_x|$  (ref. 29). Supplementary Sections 4 and 8 provide further information about the experimental setup and NV centres.

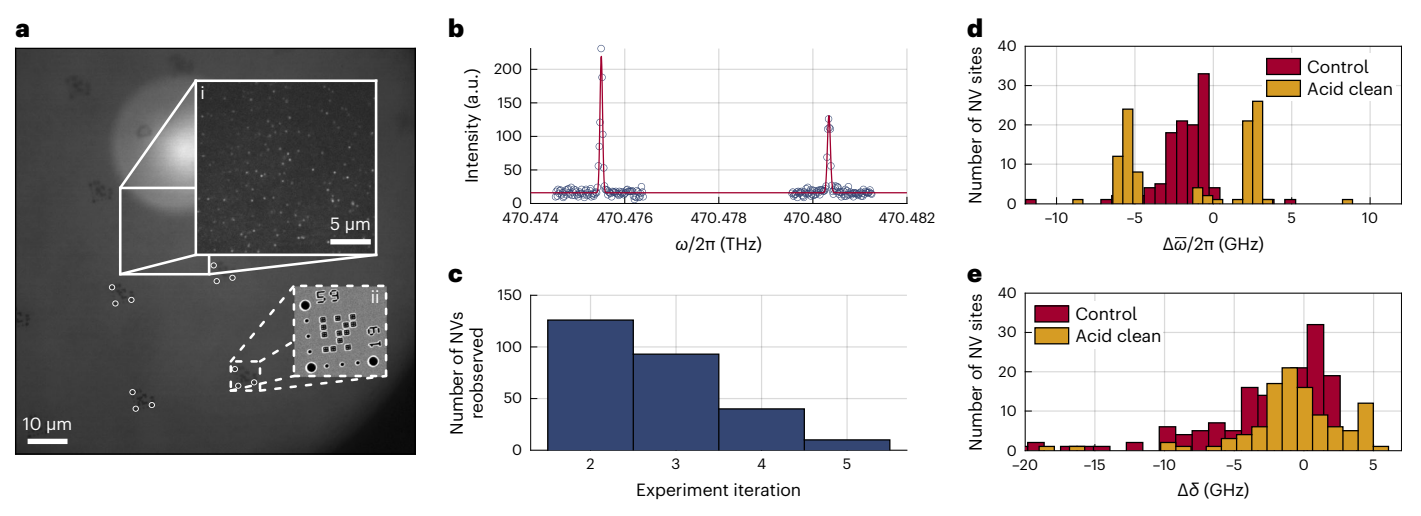


**Fig. 2** | **Tracking colour centres in a sample with fabricated QR codes. a**, Confocal microscope image of a diamond patterned with QR codes and implanted with <sup>15</sup>N. The full figure shows a confocal scan of the sample under incoherent illumination. The corners of the four QR codes are emphasized with white circles. The insets show fluorescence from part of the full field of view under 515 nm excitation with single NVs (i) and a scanning electron microscopy image of a QR code (ii). **b**, Typical PLE spectrum for an NV centre in this sample. **c**, Histogram of the number of experiments in which an NV was observed for a sample cooled down four times, with processing steps in between subsequent

experiments. Errors in clustering sites are indicated in bin 5. **d**, Visualization of the shift in mean optical transition frequency  $\Delta \bar{\omega}/2\pi = \bar{\omega}_i/2\pi - \bar{\omega}_j/2\pi$  of the two  $m_s = 0$  spin transitions between experiments j = 1 and i = 2, which served as a control, and between experiments j = 1 and i = 3, before and after tri-acid cleaning. After tri-acid cleaning, two populations of  $\bar{\omega}/2\pi$  are observed, attributable to polarization due to the presence of an electric field caused by a change in surface termination. **e**, Visualization of the shift in splitting  $\Delta \delta = \delta_i - \delta_j$  between the two  $m_s = 0$  transitions between experiments j = 1 and i = 2, which served as a control, and between experiments j = 1 and i = 3, before and after tri-acid cleaning.

Figure 2b shows a typical NV PLE spectrum. Details regarding the data analysis and QR encoding are provided in the 'Confocal data analysis' and 'QR encoding and convolutional QR detection' sections, respectively.

We track the NV centres over four experiments by registering emitters to the sample rather than to the microscope coordinates, in spite of the stochastic movement of the sample caused by remounting along with warming and cooling the system between experiments. Experiments 1 and 2 served as a control, as we thermally cycled and remounted the sample in between, but performed no additional materials processing. Between experiments 2 and 3, the sample was tri-acid cleaned in a 1:1:1 mixture of nitric, perchloric and sulfuric acids by boiling for 1 h (ref. 36) and between experiments 3 and 4, the sample was annealed in an oxygen environment at 450 °C for 4 h (ref. 37). In each experiment, NVs and QR codes were registered to the local microscope coordinate system, and then transformed into the global sample coordinate system. After registering the locations of NVs in all four experiments, we identified the NVs in each experiment that belonged to the same confocal site on the sample using a clustering algorithm constrained by a diffraction-limited Euclidean threshold distance. The number of experiments in which a colour centre was found at the same global sample coordinate site is provided in Fig. 2c: we observe that some NVs disappear over multiple experiments.

By tracking individual colour centres over multiple cryostat cooling cycles, we observe that tri-acid cleaning the diamond leads to shifts in the mean frequency at a given NV site  $\Delta\bar{\omega}/2\pi = \bar{\omega}_i/2\pi - \bar{\omega}_j/2\pi$  (for experiments i and j) of the  $m_s$  = 0 optical transitions exceeding those observed in the control. Conversely, the change in splitting  $\Delta\delta = \delta_i - \delta_j$  between the two  $m_s$  = 0 states does not deviate from the control. These observations (Fig. 2d–e) are consistent with the addition of an electric field normal to the surface  $^{29}$ , attributable to a changed surface termination  $^{38}$ . In particular, the population-level statistics for  $\bar{\omega}/2\pi$  alone do not reveal this phenomenon; tracking individual emitters uniquely enabled us to observe these minute spectral shifts.

Further, we observe that the number of reappearing NVs steadily decreases over the course of many cooling cycles (Fig. 2c). We can

classify NV sites into three categories: sites with NVs that appear in all the four cool-downs, sites with NVs that appear in 2–3 adjacent cool-downs and sites with NVs that appear in 2–3 non-adjacent cool-downs. We find that 88% of NVs found in two experiments were found in adjacent cool-downs, and 80% of the sites with NVs found in three experiments were found in adjacent cool-downs. Supplementary Section 7 shows a full accounting of NV disappearance and re-emergence. The origin of colour centre disappearance is not well understood: one possible explanation is local changes in the charge environment caused by inhomogeneities in surface termination throughout processing <sup>37–39</sup>.

#### Parallelized spectroscopy via cryogenic widefield microscopy

Although the ability to register the positions of single emitters to the surface of a sample enables individual colour centres to be tracked and compared over time, the characterization rate for the previous experiments is limited by the time to obtain one resonant PLE scan, as each site must be sequentially measured. To overcome this bottleneck, we modify our standard confocal microscope setup to excite an entire field of view with a tunable resonant laser in widefield mode (Supplementary Section 4) and thus parallelize the PLE measurements to realize a dramatic speed-up. This is made possible by the introduction of an electron-multiplying charge-coupled device camera in the imaging path, which enables us to resolve individual diffraction-limited colour centres via image processing (see the 'Widefield data analysis' section). The largest speed-up that can be achieved with this technique is set by the number of diffraction-limited emitter sites in a given field of view; the 'Advantage of widefield microscopy' section provides a detailed discussion of the regimes in which our widefield technique is faster than confocal microscopy. We demonstrate widefield PLE for two systems containing SiVs: one with an exceptionally narrow inhomogeneous distribution of optical transitions (Sample A) and one with a broad distribution (Sample B).

For Sample A, SiVs were incorporated in situ during chemical vapour deposition overgrowth on a low-strain substrate. The sample was subsequently tri-acid cleaned and annealed at 1,200 °C in ultrahigh

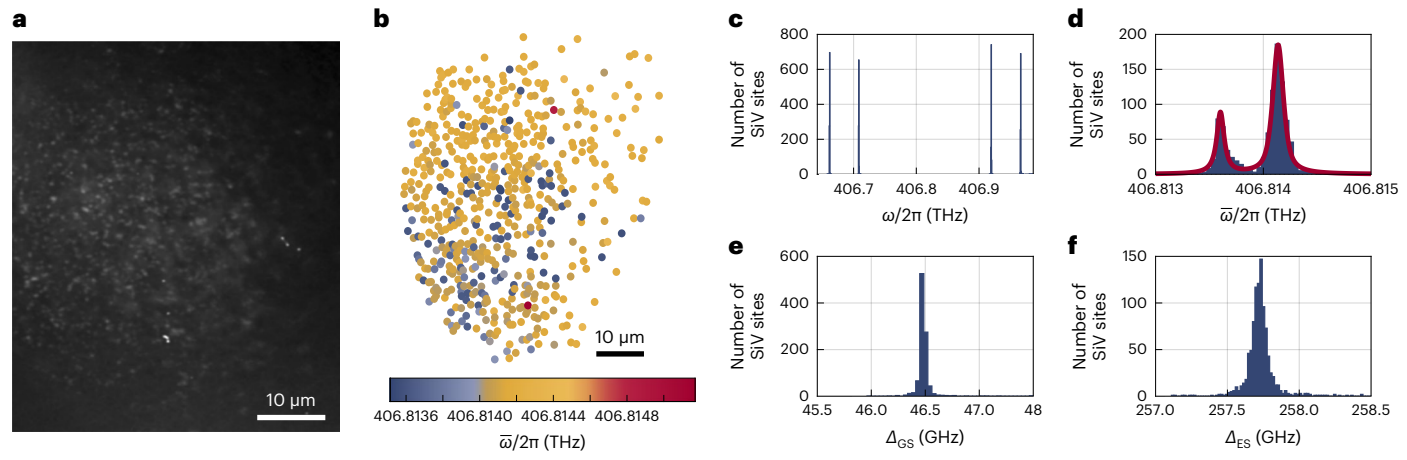


**Fig. 3** | **Widefield PLE of silicon-vacancy centres. a**, Fluorescence image of Sample A reconstructed from widefield PLE as the resonant laser frequency ω/2π was swept over 10 GHz, using the same field of view as that used elsewhere  $^{41}$ . **b**, Strain map indicating the spatial distribution of the mean ZPL transition  $\overline{ω}/2π$  (a proxy for axial strain) at 584 sites that had one PLE peak at each of the four SiV transition frequencies. We observe that the SiVs are split into two classes of axial strain. **c**, Histograms of the locations of the four optical transitions for 984 groups of SiV peaks, where each group of SiV peaks consists of a peak at each of the four SiV transition frequencies. **d**, Mean ZPL transition frequency  $\overline{ω}/2π$  for

984 groups of SiV peaks: the split into two classes of axial strain is apparent in the distribution. Fitting the empirical PDF ( $\sigma$  = 10 MHz; see the 'Empirical determination of PDFs' section) shown in red reveals a population centred at 406.8141 THz with a standard deviation of 59 MHz and a population centred at 406.8136 THz with a standard deviation of 48 MHz. **e.f.**, Ground-state splitting ( $\Delta_{GS}$ ) (**e**) and excited-state splitting ( $\Delta_{ES}$ ) (**f**) for 984 groups of SiV peaks. These splittings closely approximate the splitting due to spin–orbit coupling alone, revealing the low-strain environment.

vacuum. Figure 3a shows a fluorescence map reconstructed from widefield PLE measurements over the SiV ZPL (specifically using the ground spin-orbit-conserving Ctransition). By measuring PLE over all four SiV ZPL transitions (Supplementary Video 1), we can determine the strain environment in the overgrown layer throughout the field of view, revealing two classes (Fig. 3b-d). We ascribe this to two populations of strain along the axis of the SiV. We generate an empirical probability density function (PDF) ( $\sigma = 10 \text{ MHz}$ ; see the 'Empirical determination of PDFs' section) to determine the inhomogeneous distribution. A Gaussian fit to the empirical PDF representing  $\bar{\omega}/2\pi$ reveals a population centred at 406.8141 THz with a standard deviation of 59 MHz and a population centred at 406.8136 THz with a standard deviation of 48 MHz. Previous work has demonstrated that chemical vapour deposition growth is a promising path to generate a narrow inhomogeneous distribution of SiVs<sup>40</sup>, but to our knowledge, our measurement represents the largest number of SiVs with centre frequencies that lie within the bandwidth given by the lifetime-limited linewidth, enabling applications requiring high spectral homogeneity<sup>41</sup>. In a single field of view, we measure 257 SiV sites with ground spin-orbit C transition within  $(2\pi \times 1.7 \text{ ns})^{-1}$  from 406.7080 THz and 613 SiV sites with ground spin-orbit C transition within  $(2\pi \times 1.7 \text{ ns})^{-1}$ from 406.7085 THz. The low-transverse-strain environment is evident in the ground-state ( $\Delta_{GS}$ ) and excited-state ( $\Delta_{FS}$ ) splittings, which closely approximate the splittings due to spin-orbit coupling<sup>30</sup> (Fig. 3e,f). Supplementary Section 9 provides further information about the relationship between the SiV optical transitions and strain environment.

Given the emitter density and inhomogeneous distribution in this field of view, our widefield technique yields data on the strain environment more than 700 times faster than standard confocal microscopy (see the 'Advantage of widefield microscopy' section), saturating the limit of achievable speed-ups given the emitter density in the sample. The ability to generate strain maps via widefield PLE serves to complement and enhance other strain imaging techniques such as birefringence, which is typically measured via cross-polarization. Though the strain environment can be inferred and extrapolated from bulk birefringence measurements, widefield PLE offers a direct measure of individual spectral properties and the local strain environment.

Having demonstrated the potential for widefield PLE to generate comprehensive datasets more quickly than that possible with standard confocal PLE, we then perform widefield PLE on Sample B, where SiVs were incorporated by FIB implantation of <sup>29</sup>Si and subsequent high-temperature annealing (see the 'FIB implantation' section). Individual FIB sites are visible in a reconstructed PLE fluorescence map covering a fraction of the >1 THz inhomogeneous distribution of all the ZPL transitions (Fig. 4a).

A typical widefield PLE spectrum at one site is shown in Fig. 4c. After fitting the widefield PLE spectra at all the candidate sites, we extract the locations of 40,186 widefield PLE peaks (Fig. 4d) as well as the linewidths. We measure the widefield PLE over the entire inhomogeneous distribution, illuminating a long tail of highly strained <sup>29</sup>Si present in the FIB-implanted sites. We validate the presence of the long tail of highly strained SiVs using off-resonant PL under 515 nm illumination (Fig. 4b). To better understand the role that strain plays in SiV optical linewidths, we section the data into 20 GHz bins, and generate an empirical PDF (see the 'Empirical determination of PDFs' section) of the optical linewidths of all the peaks in each bin. We fit these data to a Gaussian distribution, and plot the mean linewidth in each frequency bin (Fig. 4e). The error bars represent one standard deviation from the mean. We find that the optical linewidths do not degrade at low optical frequencies, which is an important validation for the high-temperature operation of SiV quantum memories using highly strained emitters<sup>20</sup>.

Widefield PLE enables us to collect data for every diffraction-limited site within the field of view of our camera and within the range of our spectral scan, reducing preselection bias. This permits a more honest and comprehensive view into colour centre performance, rather than serially measuring colour centres until an emitter with the requisite optical properties for a given application is found. Beyond gaining statistics on the likelihood of finding a high-quality quantum emitter, this technique enables the large-scale characterization of materials properties in the environment surrounding the colour centres, for example, as demonstrated here by measuring the strain.

# Chip-scale verification of fabricated devices

In addition to measuring quantum emitter properties, it is also critical to be able to characterize colour centre generation. Further, thousands

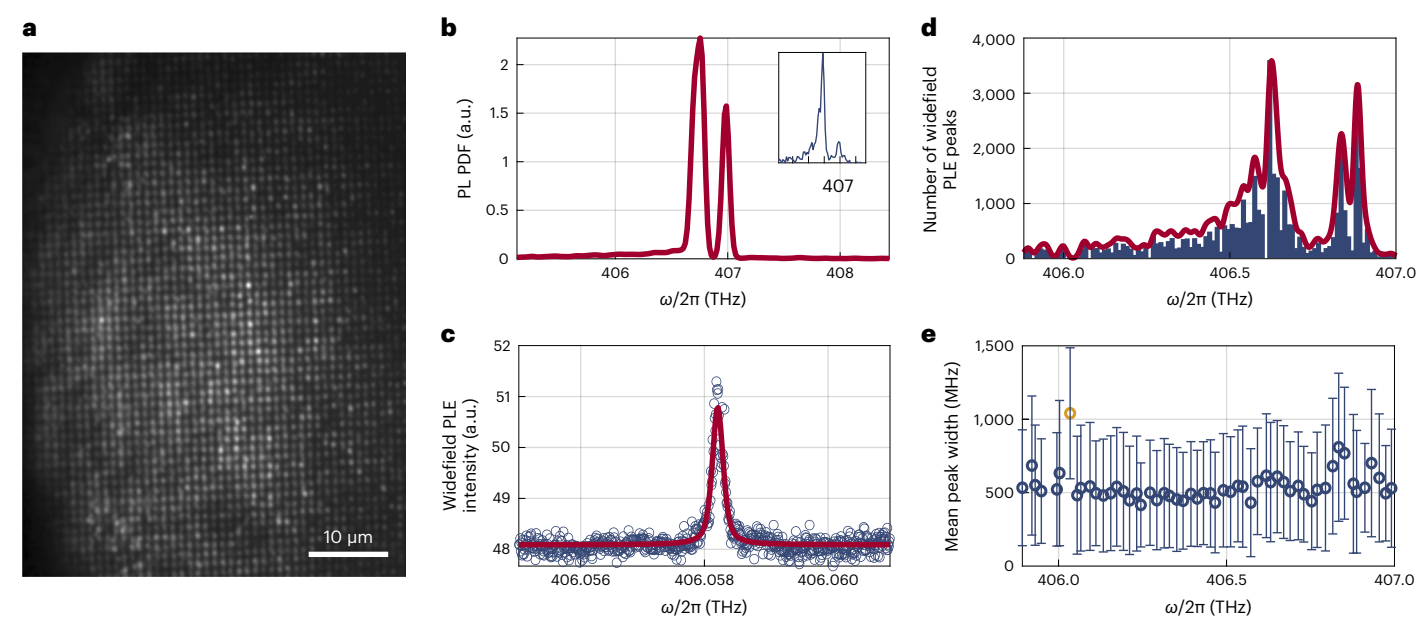


**Fig. 4** | **Widefield PLE** in a **FIB-implanted sample.** a, Fluorescence image of Sample B reconstructed from widefield PLE as the resonant laser frequency ω/2π was swept over 10 GHz. The grid of the FIB implantation sites is clearly visible. b, PDF showing the probability to find a PL peak as a function of wavelength for 11,010 SiVs confocally measured under 515 nm excitation and collected on a spectrometer. The inset shows the PL spectrum at one site. c, Typical widefield PLE spectrum of one SiV transition at one spatial site in the widefield field of view, with intensity data (blue circles) fit to a pseudo-Voigt function (red line). The fit centre location is 406.0582 THz and the fit linewidth is 210.6(1) MHz. Details of the image processing performed to extract the widefield PLE spectra can be found in the 'Widefield data analysis' section. d, Histogram showing the

inhomogeneous distribution of SiV PLE measured in widefield as a function of the resonant laser frequency  $\omega/2\pi$ . Here 40,186 peaks with linewidths less than 2 GHz and greater than the lifetime limit of  $(2\pi \times 1.7 \text{ ns})^{-1}$  are represented. A kernel estimate of the empirical PDF (see the 'Empirical determination of PDFs' section) is shown in red. **e**, Distribution of linewidths for the 40,186 peaks shown in **d**. The mean linewidth of all the peaks that line in each 20 GHz bin is shown as a blue circle. Bins containing fewer than ten peaks are shown in yellow, and discarded from the analysis. The error bars give the standard deviation of the mean. Optical linewidths do not increase at lower frequencies, indicating that the optical properties of the highly strained emitters do not degrade.

of photonic devices can be fabricated on a single chip; characterizing the properties and promise of each of these devices is time-consuming and tedious. We automate widefield imaging and spectroscopy across a  $2 \times 2$  mm<sup>2</sup> region of a diamond chip, serially stepping between the QR regions and using fluorescence to qualitatively observe the colour centres in nanopillar devices within each field of view (Supplementary Video 2). A room-temperature setup (Supplementary Section 6) with a motorized sample stage and home-built imaging processing software enables us to move from region to region, using real-time convolutional QR code detection as feedback to bring the sample into focus and compensate for variations in the sample stage motion (see the 'QR encoding and convolutional QR detection' section). Importantly, this process, and our QR detection technique, is robust against the presence of dirt or complex fabricated structures (Supplementary Videos 3 and 4). Figure 5 shows a single QR region under incoherent reflection imaging for focusing and registration, as well as under fluorescence imaging with a 532 nm excitation laser. This set of nanopillars was identified to have bright pillars at room temperature. To confirm that this technique enables the identification of colour centres that have been successfully incorporated into nanostructures, we verify that the pillars contain SiVs by measuring confocal PL under 515 nm excitation at 4 K.

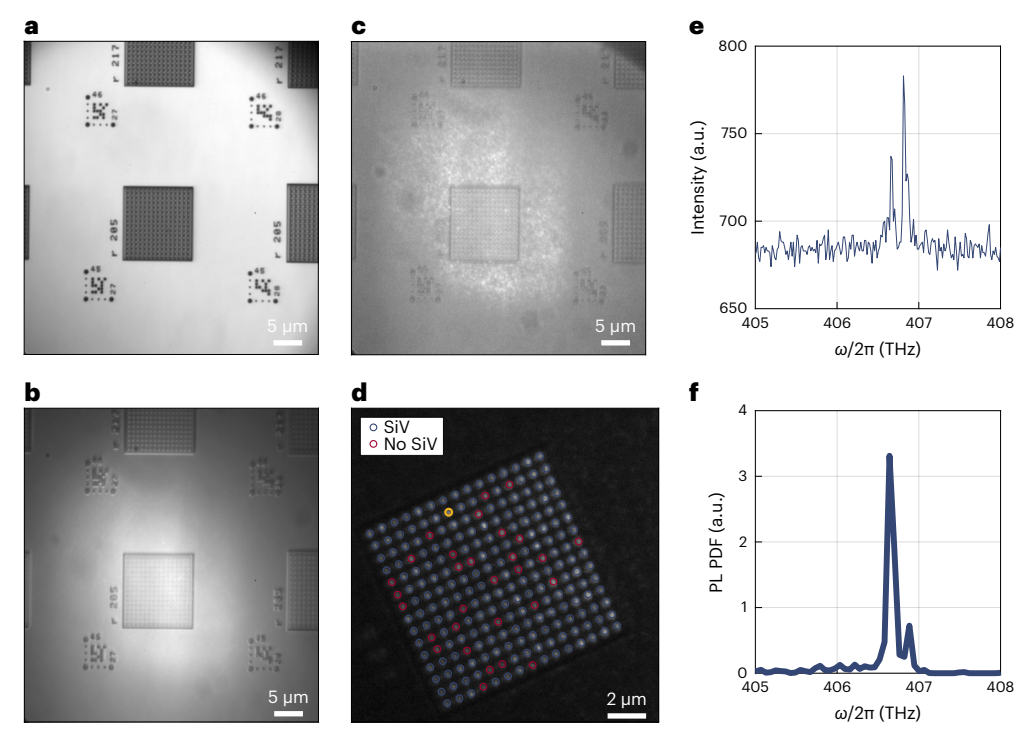
We regularly gather datasets over samples with  $\mathcal{O}(10 \text{ mm}^2)$  area, corresponding to  $\mathcal{O}(10^8)$  diffraction-limited spots. Moreover, the addition of an automated filter wheel allows us to coarsely measure the spectral content of each field of view. Supplementary Video 5 displays the data acquired with 10 nm bandpass filters around 737, 620 and 600 nm targeting silicon-, tin-, and germanium-vacancy colour centres on the red-, green- and blue-coloured channels, respectively. This imaging enables chip-scale characterization and classification to

identify promising devices and colour centres in a time-efficient and automated manner.

#### **Discussion**

Large-scale characterization of colour centres and photonic devices is necessary to scale solid-state devices from proof-of-principle demonstrations to useful technological applications. As the number of devices on chip increases to thousands or more, manual point-by-point characterization becomes intractable; our suite of automated tools performs spectroscopic measurements hundreds of times faster than traditional cryogenic confocal microscopy, opening up a new regime of system scaling. Individual colour centre tracking reveals materials-level insights into device performance, which can be used to inform and revise qubit fabrication and processing. The resultant feedback loop between design, fabrication and characterization offers a pathway to improved yields and device performance.

Furthermore, the characterization of completed devices is critical in assessing device properties and performance before integration into larger systems, a process realized at chip scale by our system. Our widefield PLE technique is compatible with existing technologies used to control the spectral properties of colour centres, such as fabricated or heterogeneously integrated strain-tuning devices<sup>30</sup>, as well as techniques for spin control such as deposited co-planar waveguides or electrodes<sup>20</sup>. Further, it is compatible with characterizing emitters in cavities: there is typically scattering out of nanophotonic structures into free-space modes due to fabrication imperfections and, in the case of suspended structures, reduced scattering into the high-index substrate. We observe emitters in nanophotonic structures under widefield off-resonant excitation at room temperature (Supplementary Video 4). Under resonant excitation, emitters located within the cavity



 $\label{eq:Fig.5} \textbf{Fig. 5} | \textbf{Chip-scale verification of fabricated devices at room temperature.} \\ \textbf{a}, \textbf{White-light image of one QR region.} \\ \textbf{b}, \textbf{PL from the region shown in a under} \\ \textbf{532} \text{ nm excitation with a longpass filter to block the excitation laser.} \\ \textbf{c}, \textbf{PL from the region shown in a under 532 nm excitation with a bandpass filter to highlight the SiV PL. Supplementary Video 2 demonstrates the automated imaging process in action over many QR regions.} \\ \textbf{d}, \textbf{Following chip-scale characterization,} \\ \end{aligned}$ 

promising regions are investigated at cryogenic temperatures. Here a confocal image of the region shown in  $\bf a$  (rotated 30° counterclockwise) is overlaid with blue circles to show pillars that contained SiVs and red circles to show pillars that did not contain SiVs.  $\bf e$ , Example PL spectrum at cryogenic temperatures from the pillar circled in yellow in  $\bf d$ .  $\bf f$ , PDF showing the probability to find a PL peak as a function of wavelength for all the pillars with SiVs shown in  $\bf d$ .

bandwidth will be enhanced, whereas emitters located outside the cavity will be suppressed. This raises an additional consideration of the cavity-emitter coupling more broadly: emitters must be spatially located in the cavity mode and spectrally within the cavity bandwidth simultaneously to achieve coupling with the cavity. Emitters that do not satisfy both requirements experience scattering off of the fabricated holes into free-space modes. In some cases, it is possible to observe cavity modes for red-detuned cavities using the phonon sideband of emitters located in the cavity mode<sup>42</sup>. Widefield PLE enables the rapid surveying of such devices to identify the best colour centre candidates to comprehensively probe. We emphasize that these techniques are readily extensible to fluorescence imaging and spectroscopy in any solid-state materials platform, including molecular qubit systems, quantum dots, other colour centre hosts and bound excitons, as well as emergent systems like emitters in two-dimensional (2D) and one-dimensional host emitters<sup>43-51</sup>, providing a basis for broad implementation.

#### Online content

Any methods, additional references, Nature Portfolio reporting summaries, source data, extended data, supplementary information, acknowledgements, peer review information; details of author contributions and competing interests; and statements of data and code availability are available at https://doi.org/10.1038/s41563-023-01644-8.

#### References

- Awschalom, D. et al. Development of quantum interconnects (QuICs) for next-generation information technologies. PRX Quantum 2, 017002 (2021).
- Alexeev, Y. et al. Quantum computer systems for scientific discovery. PRX Quantum 2, 017001 (2021).

- Sukachev, D. D. et al. Silicon-vacancy spin qubit in diamond: a quantum memory exceeding 10 ms with single-shot state readout. *Phys. Rev. Lett.* 119, 223602 (2017).
- Bar-Gill, N., Pham, L. M., Jarmola, A., Budker, D. & Walsworth, R. L. Solid-state electronic spin coherence time approaching one second. *Nat. Commun.* 4, 1743 (2013).
- Nemoto, K. et al. Photonic quantum networks formed from NV-centers. Sci. Rep. 6, 26284 (2016).
- Janitz, E., Bhaskar, M. K. & Childress, L. Cavity quantum electrodynamics with color centers in diamond. Optica 7, 1232–1252 (2020).
- 7. Siyushev, P. et al. Monolithic diamond optics for single photon detection. *Appl. Phys. Lett.* **97**, 241902 (2010).
- Hadden, J. P. et al. Strongly enhanced photon collection from diamond defect centers under microfabricated integrated solid immersion lenses. *Appl. Phys. Lett.* 97, 241901 (2010).
- 9. Mouradian, S., Wan, N. H., Schröder, T. & Englund, D. Rectangular photonic crystal nanobeam cavities in bulk diamond. *Appl. Phys. Lett.* **111**, 021103 (2017).
- Calusine, G., Politi, A. & Awschalom, D. D. Silicon carbide photonic crystal cavities with integrated color centers. *Appl. Phys. Lett.* 105, 011123 (2014).
- Nguyen, C. T. et al. An integrated nanophotonic quantum register based on silicon-vacancy spins in diamond. *Phys. Rev. B* 100, 165428 (2019).
- 12. Rugar, A. E. et al. Quantum photonic interface for tin-vacancy centers in diamond. *Phys. Rev. X* 11, 031021 (2021).
- Bayat, K., Choy, J., Baroughi, M. F., Meesala, S. & Lončar, M. Efficient, uniform, and large area microwave magnetic coupling to NV centers in diamond using double split-ring resonators. Nano Lett. 14, 1208–1213 (2014).

- Mouradian, S. L. et al. Scalable integration of long-lived quantum memories into a photonic circuit. *Phys. Rev. A* 92, 043844 (2015).
- Janitz, E. et al. Fabry-Perot microcavity for diamond-based photonics. *Phys. Rev. A* 92, 043844 (2015).
- Gould, M. et al. Large-scale GaP-on-diamond integrated photonics platform for NV center-based quantum information. J. Opt. Soc. Am. B 33, B35–B42 (2016).
- 17. Wan, N. H. et al. Large-scale integration of artificial atoms in hybrid photonic circuits. *Nature* **583**, 226–231 (2020).
- Ruf, M., Wan, N. H., Choi, H., Englund, D. & Hanson, R. Quantum networks based on color centers in diamond. J. Appl. Phys. 130, 070901 (2021).
- 19. Bradley, C. E. et al. A ten-qubit solid-state spin register with quantum memory up to one minute. *Phys. Rev. X* **9**, 031045 (2019).
- 20. Stas, P.-J. et al. Robust multi-qubit quantum network node with integrated error detection. *Science* **378**, 557–560 (2022).
- Waldherr, G. et al. Quantum error correction in a solid-state hybrid spin register. Nature 506, 204–207 (2014).
- Benjamin, S. C., Browne, D. E., Fitzsimons, J. & Morton, J. J. Brokered graph-state quantum computation. New J. Phys. 8, 141 (2006).
- Choi, H., Pant, M., Guha, S. & Englund, D. Percolation-based architecture for cluster state creation using photon-mediated entanglement between atomic memories. npj Quantum Inf. 5, 104 (2019).
- Hermans, S. L. N. et al. Qubit teleportation between non-neighbouring nodes in a quantum network. *Nature* 605, 663–668 (2022).
- Bhaskar, M. K. et al. Experimental demonstration of memory-enhanced quantum communication. *Nature* 580, 60–64 (2020).
- 26. Pompili, M. et al. Realization of a multinode quantum network of remote solid-state qubits. *Science* **372**, 259–264 (2021).
- 27. Lee, Y., Bersin, E., Dahlberg, A., Wehner, S. & Englund, D. A quantum router architecture for high-fidelity entanglement flows in quantum networks. npj Quantum Inf. 8, 75 (2022).
- Bersin, E. et al. Individual control and readout of qubits in a sub-diffraction volume. npj Quantum Inf. 5, 38 (2019).
- Bassett, L. C., Heremans, F. J., Yale, C. G., Buckley, B. B. & Awschalom, D. D. Electrical tuning of single nitrogen-vacancy center optical transitions enhanced by photoinduced fields. *Phys. Rev. Lett.* 107, 266403 (2011).
- Meesala, S. et al. Strain engineering of the silicon-vacancy center in diamond. Phys. Rev. B 97, 205444 (2018).
- Metz, J. & Barrett, S. D. Effect of frequency-mismatched photons in quantum-information processing. *Phys. Rev. A* 77, 042323 (2008).
- 32. Stolk, A. et al. Telecom-band quantum interference of frequency-converted photons from remote detuned NV centers. *PRX Quantum* **3**, 020359 (2022).
- 33. Levonian, D. et al. Optical entanglement of distinguishable quantum emitters. *Phys. Rev. Lett.* **128**, 213602 (2022).
- Walsh, M. P. Statistical Metrology and Process Control of Quantum Devices. PhD thesis, Massachusetts Institute of Technology (2020).

- 35. Chakravarthi, S. et al. Window into NV center kinetics via repeated annealing and spatial tracking of thousands of individual NV centers. *Phys. Rev. Mater.* **4**, 023402 (2020).
- 36. Chu, Y. et al. Coherent optical transitions in implanted nitrogen vacancy centers. *Nano Lett.* **14**, 1982–1986 (2014).
- Fu, K.-M., Santori, C., Barclay, P. E. & Beausoleil, R. G. Conversion of neutral nitrogen-vacancy centers to negatively charged nitrogen-vacancy centers through selective oxidation. *Appl. Phys. Lett.* 96, 121907 (2010).
- 38. Sangtawesin, S. et al. Origins of diamond surface noise probed by correlating single-spin measurements with surface spectroscopy. *Phys. Rev. X* **9**, 031052 (2019).
- 39. Yuan, Z. et al. Charge state dynamics and optically detected electron spin resonance contrast of shallow nitrogen-vacancy centers in diamond. *Phys. Rev. Res.* **2**, 033263 (2020).
- 40. Rogers, L. J. et al. All-optical initialization, readout, and coherent preparation of single silicon-vacancy spins in diamond. *Phys. Rev. Lett.* **113**, 263602 (2014).
- Christen, I. et al. An integrated photonic engine for programmable atomic control. Preprint at https://arxiv.org/ abs/2208.06732 (2022).
- 42. Day, A., Dietz, J., Sutula, M., Yeh, M. & Hu, E. L. Laser writing of spin defects in nanophotonic cavities. *Nat. Mater.* **22**, 696–702 (2023).
- Viitaniemi, M. L. K. et al. Coherent spin preparation of indium donor qubits in single ZnO nanowires. *Nano Lett.* 22, 2134–2139 (2022).
- 44. Higginbottom, D. B. et al. Optical observation of single spins in silicon. *Nature* **607**, 266–270 (2022).
- 45. Lukin, D. M. et al. 4H-silicon-carbide-on-insulator for integrated quantum and nonlinear photonics. *Nat. Photon.* **14**, 330–334 (2020).
- 46. Dietz, J. R., Jiang, B., Day, A. M., Bhave, S. A. & Hu, E. L. Spin-acoustic control of silicon vacancies in 4H silicon carbide. Preprint at https://arxiv.org/abs/2205.15488 (2022).
- Babin, C. et al. Fabrication and nanophotonic waveguide integration of silicon carbide colour centres with preserved spin-optical coherence. Nat. Mater. 21, 67–73 (2022).
- 48. Hu, X. et al. Photoluminescence of InAs/GaAs quantum dots under direct two-photon excitation. *Sci. Rep.* **10**, 10930 (2020).
- 49. Trusheim, M. E. et al. Transform-limited photons from a coherent tin-vacancy spin in diamond. *Phys. Rev. Lett.* **124**, 023602 (2020).
- 50. Davidsson, J. et al. Exhaustive characterization of modified Si vacancies in 4H-SiC. *Nanophotonics* **11**, 4565–4580 (2022).
- 51. Aharonovich, I., Englund, D. & Toth, M. Solid-state single-photon emitters. *Nat. Photon.* **10**, 631–641 (2016).

**Publisher's note** Springer Nature remains neutral with regard to jurisdictional claims in published maps and institutional affiliations.

Springer Nature or its licensor (e.g. a society or other partner) holds exclusive rights to this article under a publishing agreement with the author(s) or other rightsholder(s); author self-archiving of the accepted manuscript version of this article is solely governed by the terms of such publishing agreement and applicable law.

@ The Author(s), under exclusive licence to Springer Nature Limited 2023

#### Methods

#### **Empirical determination of PDFs**

We estimate empirical PDFs using the kernel distribution given by

$$f_k(\lambda) = \frac{1}{n} \sum_{i=1}^{n} K\left(\frac{\lambda - \lambda_i}{h}\right),\tag{1}$$

where n is the number of samples,  $\lambda_i$  are the sample values, K is a smoothing function and h is the smoothing bandwidth. We used a Gaussian smoothing function with bandwidth  $\sigma$ :

$$K(\lambda) = \exp\left(\frac{(\lambda - \lambda_{\rm c})^2}{2\sigma^2}\right)$$
 (2)

Unless otherwise noted, the bandwidth  $\sigma$  is given by our spectrometer-limited bandwidth of 0.05 nm (for photoluminescence (PL)) or the appropriate lifetime-limited linewidth (for PLE), and  $\lambda_c$  for each candidate site was set to be the centre of the fit spectra at each candidate site.

#### Confocal data analysis

To identify and characterize the colour centres, we first measure a galvanometer scan of PL excited with a strong 515 nm excitation laser (Supplementary Fig. 1a). We collect fluorescence on an avalanche photodiode in our cryogenic confocal microscope (Supplementary Section 4). We identify candidate sites by first applying a Gaussian bandpass filter to the aggregate image A(x, y), and then fit 2D Gaussians to the resulting image. First, we convolve the aggregate image with a 2D Gaussian with the lowpass standard deviation  $\sigma_{\rm D}$ :

$$f_{\rm LP}(x,y) = e^{-\frac{(x^2+y^2)}{2\sigma_{\rm LP}^2}} \tag{3}$$

We then discretize and convolve this kernel with the aggregate image I(x, y) via discrete 2D convolution to yield an intermediate filtered image R(x, y):

$$R(x,y) = \sum_{i} \sum_{j} I(i,j) f_{LP}(x-i+1,y-j+1). \tag{4}$$

We highpass filter the resulting image R(x,y) by convolution with a 2D Gaussian having highpass standard deviation  $\sigma_{\rm HP}$ :

$$f_{\rm HP}(x,y) = e^{-\frac{(x^2+y^2)}{2\sigma_{\rm HP}^2}}$$
 (5)

Finally, we discretize and convolve this kernel with the intermediate image R(x, y) via discrete 2D convolution to yield a bandpass-filtered image F(x, y):

$$F(x,y) = R(x,y) - \sum_{i} \sum_{j} R(i,j) f_{\mathsf{HP}}(x-i+1,y-j+1). \tag{6}$$

We use this Gaussian bandpass filtering process to identify bright spots with radii between the lowpass- and highpass-filter standard deviations. By fitting 2D Gaussians to the filtered image, we generate candidate emitter sites, which are stored as an array of galvanometer coordinates.

We then revisit each candidate site to determine its spectral position: we collect PL excited with a strong 515 nm laser onto a spectrometer (Supplementary Fig. 1b). We fit the spectrum taken at each candidate site and determine the centre ZPL frequency up to the resolution limit of the spectrometer. Once the spatial and coarse spectral coordinates are identified, we measure an open-loop PLE spectrum at

each candidate site using a Newport Velocity TLB-6704 laser (Supplementary Fig. 1c). Because the optical transitions of NVs are linearly polarized, we use circularly polarized resonant light to avoid biasing for one orbital state over another. We repump the emitters in between each frequency step to initialize the NVs into the ground  $m_{\rm s}=0$  state, enabling us to probe the  $E_x$  and  $E_y$  spin-conserving transitions associated with  $m_{\rm s}=0$ . The mean frequency of the ZPL transition  $\bar{v}=\bar{\omega}/2\pi$  and splitting  $\delta$  associated with the emitter at this site are also shown (Supplementary Fig. 1c). Finally, we obtain a closed-loop high-resolution scan, in which we feed back on the laser frequency using a HighFinesse WS7 Wavemeter, of each transition at every candidate site (Supplementary Fig. 1d,e).

#### Widefield data analysis

To measure the widefield PLE in Samples A and B, we swept the frequency of a Ti:sapphire excitation laser (M Squared SolsTiS) over the inhomogeneous distribution in frequency steps much smaller than the emitter lifetime, using the setup described in Supplementary Section 4. Because the optical transitions of SiVs are circularly polarized, we use linearly polarized resonant light to avoid biasing for one orbital state over another. For Sample B, a weak 515 nm Cobolt laser was continuously applied to repump the emitters. We tuned the resonator internal to the resonant laser in voltage steps that corresponded to 10 MHz steps in frequency, and locked the laser to a HighFinesse WS7 Wavemeter (60 MHz absolute accuracy, 2 MHz resolution) at each step. Once the tuning was complete, the electron-multiplying charge-coupled device was exposed for 0.5 s for Sample A and 1.0 s for Sample B.

Here we present an example of the image processing performed to extract the widefield PLE data from the raw widefield images collected. At each frequency step, the raw image was first cropped to remove the area outside the QR region (Supplementary Fig. 2a). Then, we filtered the image with a 2D Gaussian filter. We generated a 2D Gaussian kernel  $f_{\rm g}(x,y)$  with standard deviation  $\sigma$  = 2 pixels selected to approximately match the diffraction-limited spot size:

$$f_{g}(x,y) = e^{-\frac{(x^2+y^2)}{2\sigma^2}}$$
 (7)

At each frequency step  $v = \omega/2\pi$ , we discretized and convolved the kernel with the image  $M_v(x, y)$  via discrete 2D convolution to yield a filtered image  $C_v(x, y)$ :

$$C_{\nu}(x,y) = \sum_{i} \sum_{j} M_{\nu}(i,j) f_{\mathbf{g}}(x-i+1,y-j+1).$$
 (8)

Here the range of i and j in the sum spans the dimensions of the image and kernel.

After filtering each image, we sectioned the data into frequency bands to facilitate image processing. At each frequency band spanning approximately 10 GHz, we generated an aggregate image A(x,y) summarizing the fluorescence over the full band by taking the maximum value of each pixel over the images taken at all the frequency steps. An example of an aggregate image generated for images taken and scanning the resonant laser from 405.8816 to 404.9005 THz is shown in Supplementary Fig. 2b. We then used this aggregate image to identify candidate emitter sites for each frequency section, using the bandpass filtering and 2D Gaussian fitting process described previously (equations (3)–(6)). An example candidate site is circled in red in Supplementary Fig. 2a,b.

At each candidate emitter site, we determined the fluorescence intensity as a function of excitation frequency by binning the pixels around the spatial centre of the 2D Gaussian fit. An example site is shown in Supplementary Fig. 2c, with the group of binned pixels shown in a red box. Then, this group of pixels was summed at each frequency step to find the fluorescence intensity as a function of excitation

frequency  $I_{p,q}(v)$  for an emitter located at location x = p and y = q in the convolved image  $C_v(x, y)$ :

$$I_{p,q}(v) = \sum_{i=p-3}^{p+3} \sum_{j=q-3}^{q+3} C_{\nu}(i,j).$$
 (9)

We chose the number of pixels to include in the binned region to maximize the signal-to-noise ratio. Although we used the bandpass-filtered image F(x,y) to generate the candidate sites, we generated the PLE intensity function  $I_{p,q}(v)$  using the convolved images at each frequency step,  $C_v(x,y)$ . Supplementary Fig. 2d shows an example intensity function  $I_{p,q}(v)$  for the candidate SiV site. In principle, the emitter fluorescence signal  $S_{p,q}$  at a site and the background fluorescence from Sample B depend on the intensity of the excitation laser. A simple model is considered to account for fluctuating laser intensity L(v), where v is the frequency bin:

$$I_{p,q}(v) = S_{p,q}(v)L(v) + BL(v).$$
 (10)

We model this as a linear process since the emitters are driven below saturation. We determined the intensity function L(v) by calculating the average value of all the pixels in the convolved image  $C_v(x, y)$  at each frequency:

$$L(v) = \frac{1}{xy} \sum_{x} \sum_{y} C_{v}(x, y). \tag{11}$$

Although L(v) accounts for global fluctuations in intensity, it does not account for regional fluctuations, including the point spread function of the widefield microscope. Finally, we determined the frequency-dependent SiV fluorescence signal at a given site  $S_{p,q}(v)$  by dividing the measured intensity by the noise function:

$$S_{p,q}(\nu) + B = \frac{I_{p,q}(\nu)}{L(\nu)}.$$
 (12)

An example of the frequency-dependent intensity function L(v) at one site is shown in Supplementary Fig. 2e, and the final corrected signal to be fit is shown in Supplementary Fig. 2f. This model assumes that there are many colour centres such that the emission frequencies of the population of colour centres are uncorrelated, and that the dominant intensity fluctuation of the entire image is correlated with the excitation frequency.

This assumption is valid for the case of Sample B, which has a broad inhomogeneous distribution of emitters even at individual sites. However, this assumption breaks down for Sample A, since the inhomogeneous distribution is narrow. Instead, for Sample A, we use a liquid-crystal noise eater to stabilize the laser power, and fit the raw PLE data as given by equation (9).

#### QR encoding and convolutional QR detection

Custom-designed binary codes etched into the diamond surface serve as our QR-style codes. These markers consist of a 2D array of bits, with 16 bits to encode the location, 4 bits to encode a version, 1 bit as a constant pad and 3 bits as an error-detecting checksum. Supplementary Fig. 3a–c shows an example of the layout and design of these markers, a scanning electron microscopy image after the QR codes are patterned via lithography and etching and a typical optical image under our microscopes.

We make use of a convolutional approach to quickly detect and decode the position of QR markers in an image. Given the precharacterized sample rotation and scale, a kernel is generated, corresponding to the two large dots and three small dots of a single arm of the QR-code-bounding box (Supplementary Fig. 3a). Convolving a flattened version of this image with this kernel and its 90°

rotation yields two images with bright peaks corresponding to candidate positions for the horizontal and vertical arms (Supplementary Fig. 3d,e). The cubed sum of these two images leaves bright peaks at positions where both horizontal and vertical arms are detected, which are good candidates for full QR codes (Supplementary Fig. 3f). At each candidate site, the  $5\times 5$  grid that stores the coded data is binarized and decoded, with errors detected by checksum failure. Altogether, this process is efficient at extracting QR candidates and data from images (<100 ms typical processing time), to the point that real-time video data are easily processed and displayed with the detected ORs.

As an additional failsafe, we update a belief model for all the QR candidates with a positive checksum within a field of view via a majority vote, to deduce the true location and correct errors in real time. This avoids situations where false-positive checksums yield failure. Importantly, this detection procedure is also robust when other features (for example, fabricated structures) are present within the field of view (for example, Supplementary Video 4). Altogether, this robust process for real-time QR detection enables rapid feedback to the user, along with automated traversal across a sample and reliable localization of fluorescent data with the global sample coordinate system.

#### Advantage of widefield microscopy

Here we present relevant considerations when choosing between confocal and widefield microscopy, and define the regimes in which our widefield approach results in a speed-up. The time to complete a PLE experiment can widely vary depending on the specific approach: number of frequencies sampled, number of averages at each frequency point, whether a repump laser is used, microscope collection efficiency and sensor efficiency all play a role. We, therefore, define a general scheme to determine whether a parallelized widefield approach will provide a time benefit. The time to collect a confocal PLE scan at m sites in a field of view, in n frequency bins, is given by

$$t_{\text{confocal}} = m \Big( t_{\text{move}} + t_{\text{tunelaser,coarse}} + t_{\text{repump}} + n \Big( t_{\text{tunelaser,fine}} + t_{\text{collect,c}} \Big) \Big).$$
(13)

Similarly, the time to collect a PLE scan in the widefield for *m* sites in a field of view is given by

$$t_{\text{widefield}} = t_{\text{tunelaser,coarse}} + t_{\text{repump}} + n(t_{\text{tunelaser,fine}} + t_{\text{collect,w}}).$$
 (14)

These equations hold in the case of a narrow inhomogeneous distribution: if all the emitters are close in frequency and  $t_{\rm move}$  is negligible, the time to collect data for m emitters in a field of view in n frequency bins scales simply as

$$\frac{t_{\text{confocal}}}{t_{\text{widefield}}} = m \frac{t_{\text{collect,c}}}{t_{\text{collect,w}}}.$$
 (15)

As long as the integration time to collect the widefield data at each point is less than *m* times the confocal case, our widefield approach is faster.

However, this approximation breaks down for the case of a large inhomogeneous distribution. Consider the far limiting case, in which there are m emitters in the field of view that are all detuned in frequency such that they do not spectrally overlap. In this case, the time to collect data for m emitters in a field of view in n frequency bins is given by the ratio of collection times alone:

$$\frac{t_{\text{confocal}}}{t_{\text{widefield}}} = \frac{t_{\text{collect,c}}}{t_{\text{collect,w}}}.$$
 (16)

We, therefore, define an equation to determine the approximate speed-up factor (SF) of widefield over confocal PLE as a function of the number of colour centres N, the lifetime-limited linewidth  $\gamma$  and the inhomogeneous distribution  $\Gamma$ :

$$SF = N \times \frac{\gamma}{\Gamma} \times \frac{t_{\text{collect,c}}}{t_{\text{collect,w}}}.$$
 (17)

Here SF > 1 represents a speed-up for widefield over confocal microscopy.

We now calculate the value of SF for the two samples, namely, Sample A and Sample B. Sample A represents the case of a very small inhomogeneous distribution. Four widefield scans were taken in the same field of view, covering the optical excitation frequencies around the A, B, C and D transitions of the SiV in the absence of strain. All the four transitions were found at 784 diffraction-limited widefield sites, representing 3,936 PLE peaks. We note that 200 of these diffraction-limited widefield sites contained eight peaks corresponding to two groups of SiV transition frequencies, but we count only unique spatial sites in our analysis, as the transition requencies of the two SiV groups are so close in frequency. With  $t_{\rm collect,c} \approx t_{\rm collect,w}$ , and considering all the emitters lie in the same frequency bin, it would have taken SF = 784 times longer to measure the same strain distribution with our confocal microscope. For Sample B, with 40,186 peaks measured over 1.12 THz, we achieved a speed-up of SF = 4.

#### **Diamond fabrication**

The fabrication procedure of patterning QR codes is the same as the one for fabricating nanopillar arrays. Each diamond sample was first deposited with silicon nitride (hard mask) via chemical vapour deposition. The QR code and nanopillar array patterns were transferred into the nitride hard mask through electron-beam lithography and CF $_4$  reactive ion etching. Inductively coupled plasma–reactive ion etching with oxygen plasma, subsequently, transferred the mask patterns into bulk diamond. Finally, the samples were submerged in hydrofluoric acid to remove the nitride layer.

#### **FIB** implantation

We used the FIB $^{52}$  tool at the Ion Beam Laboratory (Sandia National Laboratories) to implant  $^{29}$ Si ions (spot size, -50 nm × 45 nm) at an effective areal dose of  $1 \times 10^{0}$ – $1 \times 10^{6}$  ions cm $^{-2}$ . The  $^{29}$ Si ion energy was 180 keV. After implantation, we annealed the sample at 1,200 °C in an ultrahigh-vacuum furnace. Finally, we tri-acid cleaned the sample in a 1:1:1 mixture of nitric, perchloric and sulfuric acids by boiling for 1 h.

# Data availability

The data that support the plots within this paper and other findings of this study are available from the corresponding author upon reasonable request.

#### Code availability

The code that supports the plots in this paper is available from the corresponding author upon reasonable request.

#### References

52. Schröder, T. et al. Scalable focused ion beam creation of nearly lifetime-limited single quantum emitters in diamond nanostructures. *Nat. Commun.* **8**, 15376 (2017).

# Acknowledgements

M.S. and E.B. acknowledge support from the NASA Space Technology Graduate Research Fellowship Program.

I.C. acknowledges support from the National Defense Science and Engineering Graduate Fellowship Program, the National Science Foundation (NSF) EFRI ACQUIRE program EFMA-1641064 and NSF award DMR-1747426. M.S. and M.P.W. acknowledge partial support from the NSF Center for Integrated Quantum Materials (CIQM), DMR-1231319. K.C.C. acknowledges support from the NSF RAISE-TAQS CHE-1839155 and the MITRE Corporation Moonshot program. D.R.E. acknowledges partial support from the NSF Center for Quantum Networks (CQN), EEC-1941583. Construction of the robotic cryogenic microscope was supported in part by the Air Force Office of Scientific Research under award no. FA9550-20-1-0105, supervised by G. Pomrenke. Distribution Statement A. Approved for public release. Distribution is unlimited. Diamond growth is based on work supported by the National Reconnaissance Office (NRO) under Air Force Contract no. FA8702-15-D-0001. Any opinions, findings, conclusions or recommendations expressed in this material are those of the author(s) and do not necessarily reflect the views of the National Reconnaissance Office. The FIB implantation work was performed at the Center for Integrated Nanotechnologies, an Office of Science User Facility operated for the US Department of Energy (DOE) Office of Science. Sandia National Laboratories is a multimission laboratory managed and operated by the National Technology and Engineering Solutions of Sandia, LLC, a wholly owned subsidiary of Honeywell International, Inc., for the US DOE's National Nuclear Security Administration under contract DE-NA-0003525. The views expressed in the Article do not necessarily represent the views of the US DOE or the United States government. This work made use of the Shared Experimental Facilities supported in part by the MRSEC Program of the NSF under award no. DMR-1419807.

#### **Author contributions**

M.S., I.C., E.B. and M.P.W. conceived and performed the experiments, developed the software and built the optical setups. I.C. developed the software and optical setups for widefield data collection and chip-scale sample screening. M.S. analysed the data and wrote the manuscript with assistance from I.C., E.B., M.P.W. and K.C.C. K.C.C. fabricated the QR codes designed by M.P.W. SiV Sample A was produced by J.M., A.M., S.H., D.B. and P.B.D. SiV Sample B was FIB implanted by M.T. and E.S.B. D.R.E. supervised the project. All authors discussed the results and contributed to the manuscript.

# **Competing interests**

The authors declare no competing interests.

# **Additional information**

**Supplementary information** The online version contains supplementary material available at https://doi.org/10.1038/s41563-023-01644-8.

**Correspondence and requests for materials** should be addressed to Madison Sutula.

**Peer review information** *Nature Materials* thanks the anonymous reviewers for their contribution to the peer review of this work.

**Reprints and permissions information** is available at www.nature.com/reprints.